Bifocal Metrology Applications in Space Engineering

Fulvio Bresciani, Giorgio Fasano, and János D. Pintér

1 Introduction

This chapter discusses a novel approach aimed at determining the relative attitude and position of objects. Such metrological scenarios frequently arise in applications that include robotics (collaborative robots, robotic arm control), military applications, and aeronautics (target configuration). One of the significant aeronautical applications is the autonomous landing control system for aircraft. This application is relevant, e.g., in radar-silence conditions, for the landing of ultralight aircraft, for drones in tracks without a control tower, and for aircraft carriers. Figure 1 illustrates the landing of an aircraft on an aircraft carrier, indicating the optical head (OH), and the target.

This metrological aspect is becoming increasingly important also in space engineering: consult Bresciani [1]. To accomplish the task, the technology has to provide quick and reliable measurements of the attitude and position of a spacecraft with respect to the other(s). Several examples of real-world space engineering applications entailing this advanced capability are briefly reviewed next.

The vision system of the STRONG satellite of the European Space Agency (ESA) represents a significant example. It has the scope of determining the line of sight and the range of the relative position between two or more satellites. A second

F. Bresciani (✉) · G. Fasano
Thales Alenia Space, Turin, Italy
e-mail: fulvio.bresciani@thalesaleniaspace.com; giorgio.fasano@thalesaleniaspace.com
https://www.thalesgroup.com/en

J. D. Pintér
Department of Management Science and Information Systems, Rutgers Business School - New Brunswick Campus, Rutgers University, Piscataway, NJ, USA
e-mail: jpinter@business.rutgers.edu

G. Fasano, J. D. Pintér (eds.), *Modeling and Optimization in Space Engineering*,
Springer Optimization and Its Applications 200,
https://doi.org/10.1007/978-3-031-24812-2_4

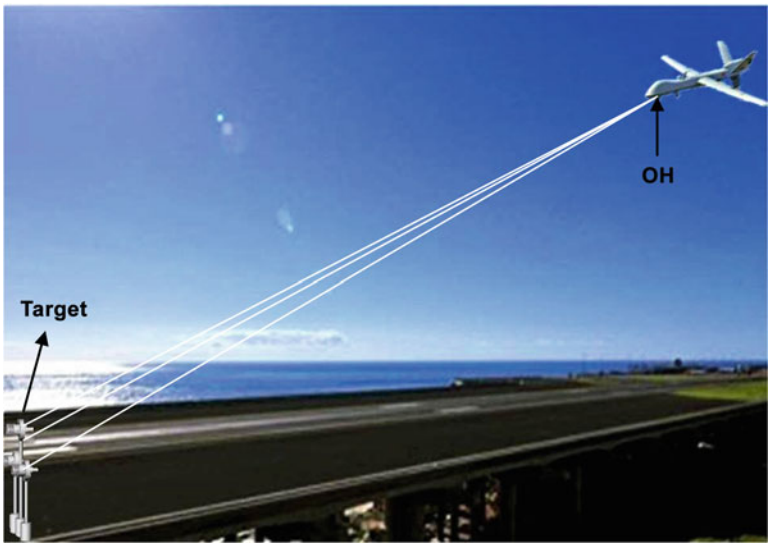

Fig. 1 Aircraft landing on an aircraft carrier

example of interest concerns PROBA-3, ESA's first precision formation flying mission. A pair of satellites fly together maintaining a fixed configuration as a "large rigid structure" in space to investigate formation-flying technologies. Conceptually, the PROBA-3 mission consists of two independent, three-axis stabilized mini satellites flying in a formation with relative position control accuracy of less than 1 mm, see Fig. 2. The two mini satellites are referred to as Coronograph SpaceCraft (CSC) with metric dimensions of $1.1 \times 1.8 \times 1.7$ m^3, and Occulter SpaceCraft (OSC) with dimensions of $0.9 \times 1.4 \times 0.9$ m^3. The paired satellites jointly form a 150-meter-long solar coronagraph to study the Sun's faint corona more closely to the solar rim than has ever been achieved before.

A further noteworthy example is the Magsat program, a joint project by the National Aeronautics and Space Administration (NASA) and the United States Geological Survey (USGS) to measure near-earth magnetic fields on a global basis. The spacecraft consisted of two distinct parts, see Fig. 3: the instrument module that contains a vector and a scalar magnetometer, in addition to its unique basis apparatus; and the base module that contains the data-handling, power, communication, command, and attitude-control subsystems to support the instrument module. The magnetometers were deployed after launch, using a deployable scissor boom, to a position of 6 m behind the spacecraft. At this distance, the influence of magnetic materials from the instrument and base module was less than 1 nanotesla. The directional accuracy of the vector magnetometer was required to be of 20 arc seconds in all three axes (coordinates). The related error allocation analysis determined that the attitude control subsystem was required to yield an accuracy of 7 arc seconds per axis to meet the overall system requirements. The performance

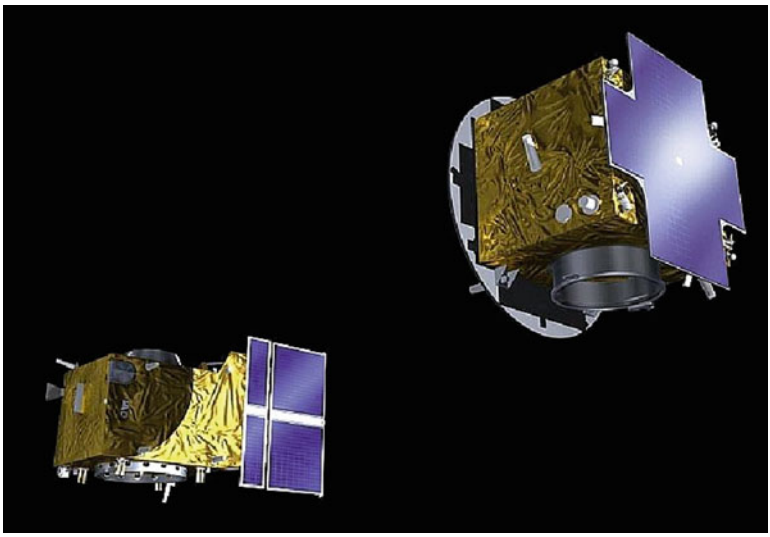

Fig. 2 PROBA-3 CSC (left) and OSC (right). (Credits: ESA)

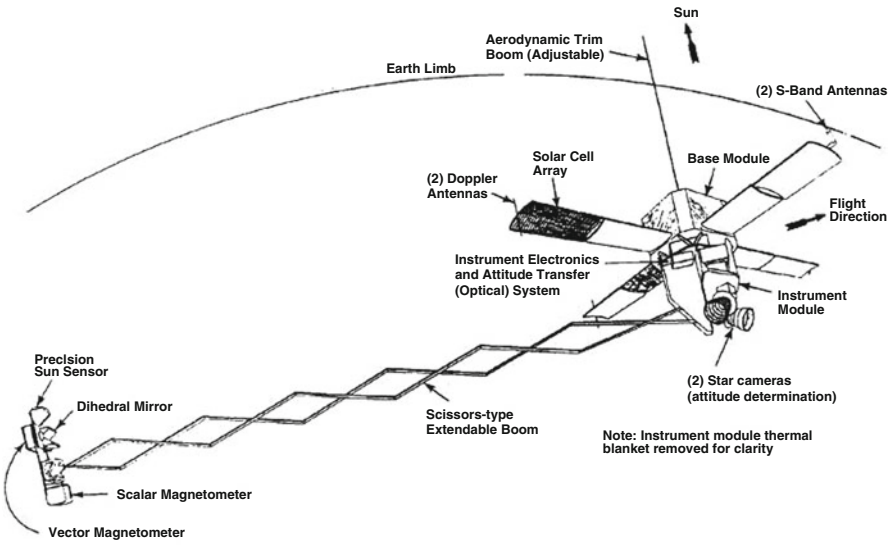

Fig. 3 Magsat orbital configuration. (Credits: NASA)

goal was set to 1 arc second for pitch and yaw, and 5 arc seconds for twist (roll). The pitch-yaw acquisition range required was $\pm 0.5°$ as a goal, with a precision range over ± 3 arc minutes. The twist system required a precision range of $\pm 0.08°$ over the pitch-yaw precision range. Moreover, the dynamic range in the magnetometer platform displacement motion was set to $\pm 0.25°$ in any transverse direction.

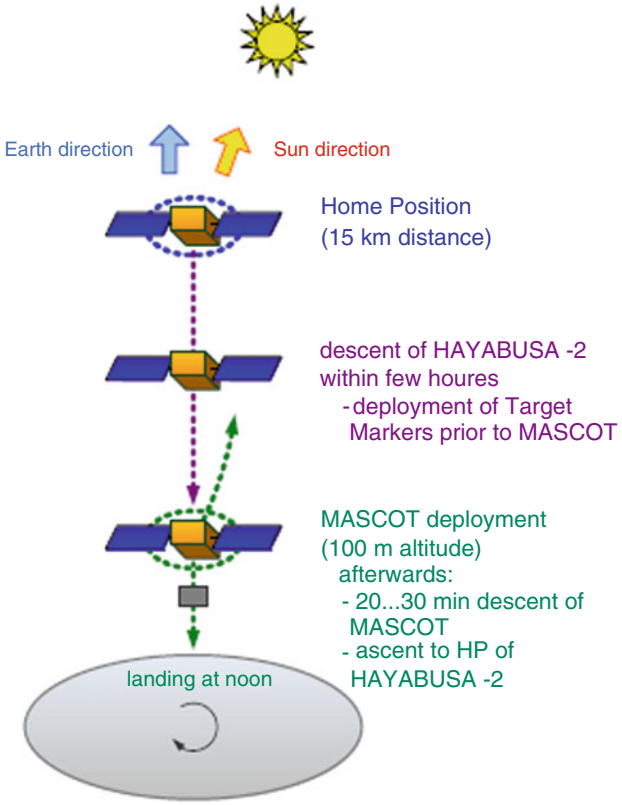

Fig. 4 HAYABUSA-2 deployment phase (left) and MASCOT separation (right). (Credits: JAXA)

Another interesting application is represented by HAYABUSA-2, an asteroid exploration mission by the Japanese Space Exploration Agency (JAXA), aimed at studying Asteroid 1999 JU3. The spacecraft deploys the MASCOT lander built in Europe for an in situ study of surface composition and properties, see Fig. 4. The landing site is selected prior to the MASCOT deployment by evaluating the global asteroid map, but restricted to the illuminated asteroid side. During a sampling "dress rehearsal" maneuver, the main spacecraft descends from its home position (HP) to an altitude of approximately 100 m and deploys the lander by initializing a proper delta-v (Δv) through the separation mechanism. The lander then freefalls to the surface, while HAYABUSA-2 ascends back to its HP located at a distance of 15 km. During the first phase, after being released, MASCOT reaches the asteroid. Here, the metrological aspects are particularly demanding due to the requested accuracy. Similar scenarios occur, e.g., in active debris removal, object rendezvous, and formation-flying.

The OCSD (Optical Communications and Sensor Demonstration) program is the first in a new series of six NASA-managed demonstration missions adopting

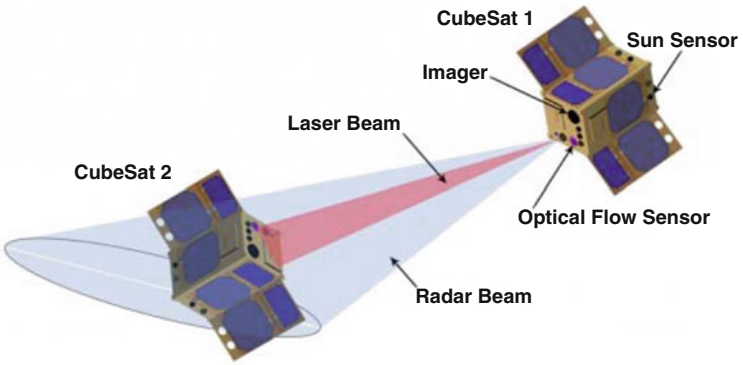

Fig. 5 Two CubeSats in close proximity operations. (Credits: Aerospace Corp)

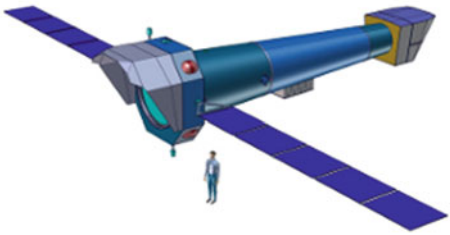

Fig. 6 Athena telescope. (Credits: ESA Concurrent Design Facility)

CubeSat to test technologies that enable new uses of these miniature satellites, measuring approximately $10 \times 10 \times 10$ cm^3. The first mission is a technical demonstration of the various systems testing the laser communication terminal. The next two satellites will be deployed as a pair to demonstrate the ability to maneuver small spacecraft in close proximity (approximately 200 m) to one another using low-cost sensors and a novel water propulsion, see Fig. 5. This technology can enhance the ability of small spacecraft to work in coordination with other satellites to explore asteroids, planets, and moons, as well as inspecting other spacecraft.

The Athena (Advanced Telescope for High-ENergy Astrophysics) mission of ESA, see https://sci.esa.int/web/athena, is selected in this chapter as a specific case study for the innovative metrological approach proposed. Athena is based on an X-ray telescope (see Fig. 6) designed to address the Cosmic Vision science theme "The Hot and Energetic Universe." This satellite will utilize a telescope with a 12-m focal length and two primary instruments: the high-resolution X-ray Integral Field Unit (X-IFU) and the Wide Field Imager (WFI) featuring a moderate resolution and a large field of view. The high-precision measurement of the telescope line of sight (LoS) internal misalignments is crucial. The on-board metrological instrument is expected to be placed as close as possible to the node and focal plane center of the telescope mirror to detect at a very high precision the errors in the LoS vector, due to inevitable thermal distortions.

Metrological problems of the type illustrated above are usually tackled by adopting very complex systems that often use different technologies in parallel: for optical metrology, consult, e.g., Tyson [13] and Yoshizawa [14]. The most frequently used metrological solutions considered in space applications include the Universal Lateral and Longitudinal Integrated Sensor (ULLIS), Hexa-Dimensional Optical Metrology (HDOM), ATV Videometer, and Rendezvous Laser Vision System (RELAVIS).

- The Universal Lateral and Longitudinal Integrated Sensor (ULLIS) is a sensor composed of a detector, an optical system, and an electronic unit on one side, in addition to a set of retroreflectors on the other side. This device has the capability to measure both the lateral and longitudinal positions of one side with respect to the other.
- The Hexa-Dimensional Optical Metrology (HDOM) is a metrological system aimed at providing the 3D-position and 3D-attitude of one side with respect to the reference frame of another side.
- The ATV Videometer is a metrological system based on visual techniques utilized to support the docking of the Automated Transfer Vehicle (ATV, ESA) to the International Space Station (ISS).
- The Rendezvous Laser Vision System (RELAVIS) is a system designed to support autonomous space operations. RELAVIS provides accurate detection, tracking, and estimation of spacecraft for rendezvous-docking operations, satellite inspection, and servicing operations.

A promising alternative approach is based on the innovative bifocal concept, see Bresciani and Musso [2–4]. This system is characterized by a double optical train, which yields information about position and attitude of an object with respect to another, for all six degrees of freedom. It covers a variable range of possible distances, i.e., from ten meters to tens of kilometers, depending on the application and measurement purpose. In the specific case of space engineering (the application field considered in this chapter), the bifocal metrological systems can provide precise information about the mutual position and attitude of two spacecraft in a short, medium, and far range involving only one sensor and covering either fine or coarse accuracies. In fact, the bifocal metrology is the first optical projective system able to tackle six degrees of freedom metrological scenarios that adopts a single sensor. A simple analytical algorithm solves the related six degrees of freedom problem without the need for high computing power. The optical system is very simple and compact: in addition to the light target, composed by only three Light Emitted Diodes (LEDs), has no particular complexity in terms of volume accommodation, technological developments, space qualifications, and on-ground characterization. All the components of this metrological system can be selected among the already space-qualified items.

These key aspects of the bifocal metrology with respect to the existing metrologies make the new approach suitable for a wide range of space applications: rendezvous and docking, co-orbiting satellites, large space instruments based on formation flying technology, extendable structures, and CubeSat networks.

The remainder of this chapter is structured as follows. Section 2 presents the bifocal system concept. Section 3 is dedicated to the mathematical aspects, concerning the projected image generation, the inverse problem of reconstructing the target position and attitude by the projected image measurement, the analytical solution, and the relative error analysis. Section 4 discusses two optimization problems regarding the bifocal system sizing and the light spot shaping, respectively. A real-world application is illustrated in Sect. 5, and conclusions are presented in Sect. 6.

2 Bifocal System Concept

The bifocal system discussed here consists of the following components:

- A light target consisting of three LEDs placed at the vertices of an isosceles triangle.
- A two-channel optical head (each channel with its own focal length) that focuses the light target image on an image sensor.

The working principle of the system is shown in Fig. 7, when two spacecrafts denoted by S1 and S2 are considered. The optical head consisting of the optical trains OT1 and OT2 is installed on S1, and the three LEDs are positioned on S2.

The joint presence of two focal lengths allows using the device as a single focal metrology system with different operative ranges (coarse metrology) or as a metrology system with a better accuracy than a classical projection metrology

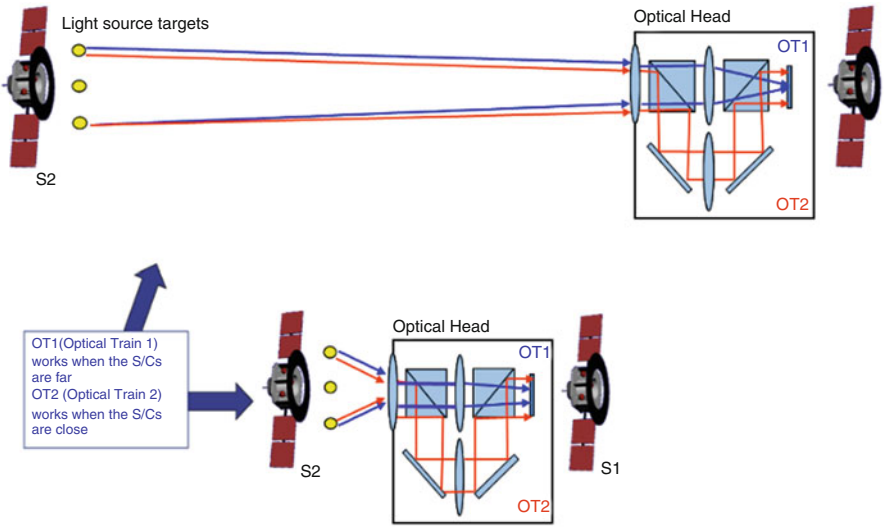

Fig. 7 Bifocal system: basic concept

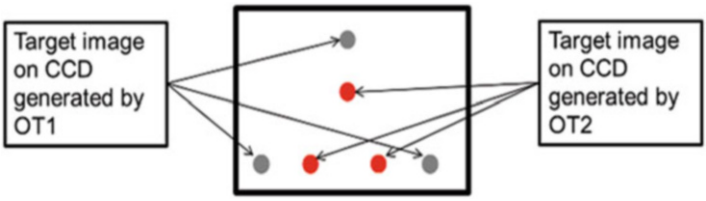

Fig. 8 CCD target image projection

system (fine metrology). When the spacecrafts are either far or close, a coarse measurement can be performed. When both target images are projected on the image sensor (charged coupled device, CCD) a refined measurement can be carried out: see Fig. 8.

Considering the target light spots (three for each optical channel) on the projected image plane, through a simple mathematical algorithm requiring little computing power, it is possible to determine the position and attitude accurately (considering six degrees of freedom, including the roll, pitch, and yaw angles), with respect to the optical head.

3 Mathematical Model

In this section, the analytical computation of position and attitude of a generic target with respect to all the six degrees of freedom using a bifocal optical system is described: for further details, consult Bresciani and Musso [2–4].

3.1 3D-Transformation Matrix

Consider an orthogonal right-handed 3D-coordinate system with origin O and axes x, y, and z. Angular rotations around the axes x, y, and z can be represented by the following rotation matrices, see, e.g., Ghali [6]:

$$R_x(\theta) = \begin{bmatrix} 1 & 0 & 0 & 0 \\ 0 & \cos\theta & \sin\theta & 0 \\ 0 & -\sin\theta & \cos\theta & 0 \\ 0 & 0 & 0 & 1 \end{bmatrix}, \tag{1-1}$$

$$R_y(\beta) = \begin{bmatrix} \cos\beta & 0 & -\sin\beta & 0 \\ 0 & 1 & 0 & 0 \\ \sin\beta & 0 & \cos\beta & 0 \\ 0 & 0 & 0 & 1 \end{bmatrix}, \tag{1-2}$$

$$R_z(\gamma) = \begin{bmatrix} \cos\gamma & \sin\gamma & 0 & 0 \\ -\sin\gamma & \cos\gamma & 0 & 0 \\ 0 & 0 & 1 & 0 \\ 0 & 0 & 0 & 1 \end{bmatrix}, \tag{1-3}$$

where θ, β, and γ are the rotation angles with respect to x, y, and z.

The 3D-translation matrix is defined by

$$T_{xyz}(\Delta x, \Delta y, \Delta z) = \begin{bmatrix} 1 & 0 & 0 & 0 \\ 0 & 1 & 0 & 0 \\ 0 & 0 & 1 & 0 \\ \Delta x & \Delta y & \Delta z & 1 \end{bmatrix}, \tag{2}$$

where Δx, Δy, and Δz are the displacements along the axes x, y, and z, respectively.

Rotations and translations are applied to a point with coordinates (X, Y, Z) by the following transformation:

$$\begin{aligned} \left[X', Y', Z', 1\right] &= [X, Y, Z, 1]\, R_x(\theta)\, R_y(\beta)\, R_z(\gamma)\, T_{xyz}(\Delta x, \Delta y, \Delta z) \\ &= [X, Y, Z, 1]\, M(\theta, \beta, \gamma, \Delta x, \Delta y, \Delta z) \end{aligned} \tag{3}$$

Here (X, Y, Z) is the original point, and (X', Y', Z') is the point after the roto-translation shown above. The matrix $M(\theta, \beta, \gamma, \Delta x, \Delta y, \Delta z) = R_x(\theta)\, R_y(\beta)\, R_z(\gamma)\, T_{xyz}(\Delta x, \Delta y, \Delta z)$ can be expressed as

$$M(\theta, \beta, \gamma, \Delta x, \Delta y, \Delta z) = \begin{bmatrix} \cos\gamma\cos\beta & \sin\gamma\cos\beta & -\sin\beta & 0 \\ \sin\theta\sin\beta\cos\gamma - \sin\gamma\cos\theta & \sin\gamma\sin\beta\sin\theta + \cos\gamma\cos\theta & \sin\theta\cos\beta & 0 \\ \cos\theta\sin\beta\cos\gamma - \sin\gamma\sin\theta & \sin\gamma\sin\beta\cos\theta - \cos\gamma\sin\theta & \cos\theta\cos\beta & 0 \\ \Delta x & \Delta y & \Delta z & 1 \end{bmatrix} \tag{4}$$

Hence, the explicit form of Eq. (3) is

$$\left[X', Y', Z', 1\right] = [X, Y, Z, 1] \begin{bmatrix} \cos\gamma\cos\beta & \sin\gamma\cos\beta & -\sin\beta & 0 \\ \sin\theta\sin\beta\cos\gamma - \sin\gamma\cos\theta & \sin\gamma\sin\beta\sin\theta + \cos\gamma\cos\theta & \sin\theta\cos\beta & 0 \\ \cos\theta\sin\beta\cos\gamma - \sin\gamma\sin\theta & \sin\gamma\sin\beta\cos\theta - \cos\gamma\sin\theta & \cos\theta\cos\beta & 0 \\ \Delta x & \Delta y & \Delta z & 1 \end{bmatrix} \tag{5}$$

The transformation shown above is used as a basic underlying concept for the optical application discussed in this chapter. Prior to introducing the bifocal

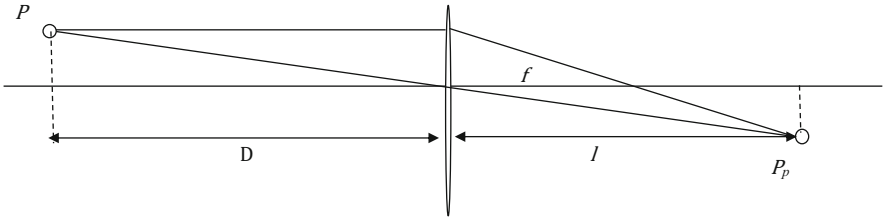

Fig. 9 Mono-focal projective system

approach, the mono-focal case is outlined, consisting of a simple optical projective system. In this scenario, the relationship between the object P and its projected image P_p is illustrated in Fig. 9.

In Fig. 9, D is the horizontal distance between the target point P and the lens utilized, while l is the horizontal distance between the lens center and the projection P_p. The distance between the lens focus and the projection is denoted by f. The axes x and y of the right-handed reference frame (x, y, z) considered here lie on the projection plane (y is the vertical axis); the axis z (oriented toward the target point P) is parallel to D and l. The following expression holds:

$$P_\mathrm{p}\left(X_\mathrm{P}, Y_\mathrm{P}, Z_\mathrm{P}\right) = P_\mathrm{p}\left(\frac{lX}{D}, \frac{lY}{D}, 0\right) \tag{6}$$

where (X, Y, Z) are the coordinates of the target point P.

Considering the relation (6), Eq. (5) links the image point $P_\mathrm{p}(X_\mathrm{P}, Y_\mathrm{P}, Z_\mathrm{P})$ and the corresponding $P'_\mathrm{p}(X'_\mathrm{P}, Y'_\mathrm{P}, Z'_\mathrm{P})$ obtained by the rotations θ, β, and γ and the displacements Δx, Δy, and Δz along the axes. The following equation holds:

$$\left[X'_\mathrm{P}, Y'_\mathrm{P}, 0, \frac{l}{D}\right] = \frac{l}{D}\left[X, Y, 0, 1\right] \begin{bmatrix} \cos\gamma\cos\beta & \sin\gamma\cos\beta & -\sin\beta & 0 \\ \sin\theta\sin\beta\cos\gamma - \sin\gamma\cos\theta & \sin\gamma\sin\beta\sin\theta + \cos\gamma\cos\theta & \sin\theta\cos\beta & 0 \\ \cos\theta\sin\beta\cos\gamma - \sin\gamma\sin\theta & \sin\gamma\sin\beta\cos\theta - \cos\gamma\sin\theta & \cos\theta\cos\beta & 0 \\ \Delta x & \Delta y & \Delta z & 1 \end{bmatrix}. \tag{7}$$

3.2 Bifocal Problem Statement

The bifocal system discussed in this chapter is depicted schematically by Fig. 10. Here ***A*** is the target and ***B*** details the positions of the three light sources $P_1(X_1, Y_1, Z_1)$, $P_2(X_2, Y_2, Z_2)$, $P_3(X_3, Y_3, Z_3)$ selected as the target. ***C*** represents the bifocal optical system as a whole (optical head), consisting of two equal-size lenses and

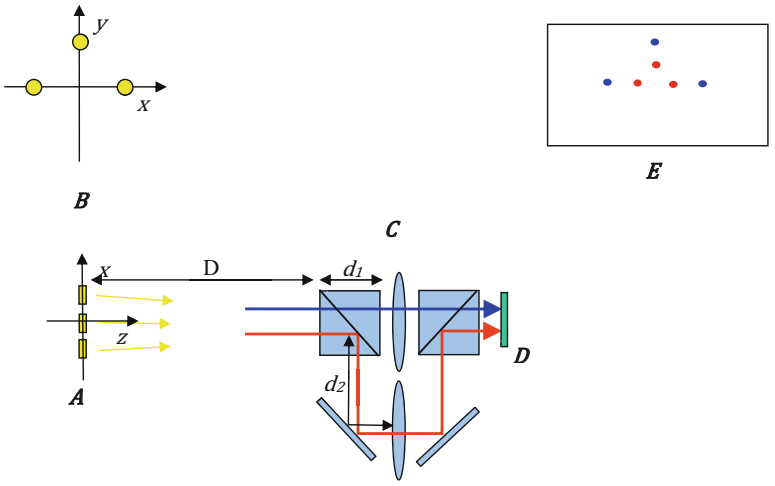

Fig. 10 Schematic representation of a bifocal system

four mirrors. ***D*** and ***E*** are the perpendicular and parallel views, respectively, of the image plane.

The bifocal system is, in fact, a combination of two mono-focal systems involving lenses 1 and 2, with l_1 and l_2 as the corresponding internal optical lengths. The two generated images (colored in blue and red for lenses 1 and 2) have the magnitudes $M(f_1)$ and $M(f_2)$, depending on the focal distances f_1 and f_2, respectively. The two associated sets of projected points, generated by the target three (light-)points for lenses 1 and 2 are denoted by $P_{1p1}(X_{1p1}, Y_{1p1}, Z_{1p1})$, $P_{2p1}(X_{2p1}, Y_{2p1}, Z_{2p1})$, $P_{3p1}(X_{3p1}, Y_{3p1}, Z_{3p1})$, and $P_{1p2}(X_{1p2}, Y_{1p2}, Z_{1p2})$, $P_{2p2}(X_{2p2}, Y_{2p2}, Z_{2p2})$, $P_{3p2}(X_{3p2}, Y_{3p2}, Z_{3p2})$.

The general bifocal problem consists of determining the position and attitude of a target (identified by three light sources) with respect to a given initial condition, by measuring the positions of the corresponding projected six points generated by the bifocal system. Specifically, it is assumed that the initial positions of the three target (light-)points $P_1(X_1, Y_1, Z_1)$, $P_2(X_2, Y_2, Z_2)$, $P_3(X_3, Y_3, Z_3)$ are known with respect to the assigned reference frame (associated with the bifocal optical head), as well as their projected images $P_{1p1}(X_{1p1}, Y_{1p1}, Z_{1p1})$, $P_{2p1}(X_{2p1}, Y_{2p1}, Z_{2p1})$, $P_{3p1}(X_{3p1}, Y_{3p1}, Z_{3p1})$, and $P_{1p2}(X_{1p2}, Y_{1p2}, Z_{1p2})$, $P_{2p2}(X_{2p2}, Y_{2p2}, Z_{2p2})$, $P_{3p2}(X_{3p2}, Y_{3p2}, Z_{3p2})$, generated by lenses 1 and 2. After rotations θ, β, and γ of the target (around the axes x, y, and z, respectively), and displacements Δx, Δy, and Δz of the target along the axes x, y, and z, the projected points $P'_{1p1}(X'_{1p1}, Y'_{1p1}, Z'_{1p1})$, $P'_{2p1}(X'_{2p1}, Y'_{2p1}, Z'_{2p1})$, $P'_{3p1}(X'_{3p1}, Y'_{3p1}, Z'_{3p1})$, generated by lens 1, are correlated with the corresponding initial projected points $P_{1p1}(X_{1p1}, Y_{1p1}, Z_{1p1})$, $P_{2p1}(X_{2p1}, Y_{2p1}, Z_{2p1})$, $P_{3p1}(X_{3p1}, Y_{3p1}, Z_{3p1})$, generated by lens 1, by three equations having the general form of Eq. (5). Similarly, three equations of the general form of Eq. (5) relate the new projected points $P'_{1p2}(X'_{1p2}, Y'_{1p2}, Z'_{1p2})$, $P'_{2p2}(X'_{2p2}, Y'_{2p2}, Z'_{2p2})$, $P'_{3p2}(X'_{3p2},$

Y'_{3p2}, Z'_{3p2}), generated by lens 2, with the corresponding initial projected images $P_{1p1}(X_{1p1}, Y_{1p1}, Z_{1p1})$, $P_{2p1}(X_{2p1}, Y_{2p1}, Z_{2p1})$, $P_{3p1}(X_{3p1}, Y_{3p1}, Z_{3p1})$ generated by lens 2.

In general, a roto-translation of the target θ, β, γ, Δx, Δy, and Δz (with respect to the known initial condition) can be expressed by a system of six equations of the form of Eq. (5), each corresponding to one of the projected points $P'_{1p1}(X'_{1p1}, Y'_{1p1}, Z'_{1p1})$, $P'_{2p1}(X'_{2p1}, Y'_{2p1}, Z'_{2p1})$, $P'_{3p1}(X'_{3p1}, Y'_{3p1}, Z'_{3p1})$, $P'_{1p2}(X'_{1p2}, Y'_{1p2}, Z'_{1p2})$, $P'_{2p2}(X'_{2p2}, Y'_{2p2}, Z'_{2p2})$, and $P'_{3p2}(X'_{3p2}, Y'_{3p2}, Z'_{3p2})$. The bifocal problem consists of inverting this system of equations so that the new configuration of the target (with respect to the initial condition), expressed by θ, β, γ, Δx, Δy, and Δz can be derived by the direct measurements of the projected points shown above: here we assume that $P_{1p1}(X_{1p1}, Y_{1p1}, Z_{1p1})$, $P_{2p1}(X_{2p1}, Y_{2p1}, Z_{2p1})$, and $P_{3p1}(X_{3p1}, Y_{3p1}, Z_{3p1})$ are known.

3.3 Mathematical Solution

In order to solve the inverted system of equations introduced in Sect. 3.2, as per the initial conditions, the three target light-points are specified with respect to the optical head reference frame as follows:

$$P_1\,(X_1, Y_1, Z_1) = (X_0, 0, 0)\,,$$
$$P_2\,(X_2, Y_2, Z_2) = (-X_0, 0, 0)\,,$$
$$P_3\,(X_3, Y_3, Z_3) = (0, Y_0, 0)\,.$$

As shown above, P_1 and P_2 are placed (symmetrically) along the x-axis at a distance X_0 from the origin, while P_3 is on the y-axis at a distance Y_0 from the origin. Since P_1 and P_2 are not affected by rotations around the x axis, Eq. (5) can be applied to both corresponding projected points, obtained either by lens 1 or 2, by adopting the simplifying condition $\theta = 0$. This yields the following specific equations for the projections P'_{1p1} and P'_{2p1}:

$$\left[X'_{1p1}, Y'_{1p1}, 0, \frac{l_1}{D+d_1}\right] = \frac{l_1}{D+d_1}\,[X_0, 0, 0, 1]\begin{bmatrix} \cos\gamma\,\cos\beta & \sin\gamma\,\cos\beta & -\sin\beta & 0 \\ -\sin\gamma & \cos\gamma & 0 & 0 \\ \sin\beta\,\cos\gamma & \sin\gamma\,\sin\beta & \cos\beta & 0 \\ \Delta x & \Delta y & \Delta z & 1 \end{bmatrix}, \tag{8-1}$$

$$\left[X'_{2p1}, Y'_{2p1}, 0, \frac{l_1}{D+d_1}\right] = \frac{l_1}{D+d_1}\,[-X_0, 0, 0, 1]\begin{bmatrix} \cos\gamma\,\cos\beta & \sin\gamma\,\cos\beta & -\sin\beta & 0 \\ -\sin\gamma & \cos\gamma & 0 & 0 \\ \sin\beta\,\cos\gamma & \sin\gamma\,\sin\beta & \cos\beta & 0 \\ \Delta x & \Delta y & \Delta z & 1 \end{bmatrix}, \tag{8-2}$$

where $D + d_1$ is the working distance of lens 1. After algebraic manipulations that are omitted, the following equations are obtained:

$$\Delta X'_{12p1} = \frac{2l_1}{D + d_1} X_0 \cos\gamma \cos\beta, \tag{9-1}$$

$$\Delta Y'_{12p1} = \frac{2l_1}{D + d_1} X_0 \sin\gamma \cos\beta, \tag{9-2}$$

where $\Delta X'_{12p1} \equiv X'_{1p1} - X'_{2p1}$ and $\Delta Y'_{12p1} \equiv Y'_{1p1} - Y'_{2p1}$. Further technical details concerning the mathematical formulation outlined here are presented by Bresciani and Musso [2–4].

Operating exactly the same way as lens 1, for lens 2 analogous equations are obtained:

$$\Delta X'_{12p2} = \frac{2l_2}{D + d_2} X_0 \cos\gamma \cos\beta, \tag{10-1}$$

$$\Delta Y'_{12p2} = \frac{2l_2}{D + d_2} X_0 \sin\gamma \cos\beta, \tag{10-2}$$

where $\Delta X'_{12p2} = X'_{1p2} - X'_{2p2}$ and $\Delta Y'_{12p2} = Y'_{1p2} - Y'_{2p2}$.

Combining (9-1), (9-2), (10-1), and (10-2) yields the following relations:

$$\gamma = a\tan\left(\frac{\Delta Y'_{12p1}}{\Delta X'_{12p1}}\right), \tag{11}$$

$$D = \frac{l_1 d_2 \Delta X'_{12p2} - l_2 d_1 \Delta X'_{12p1}}{l_1 \Delta X'_{12p1} - l_2 \Delta X'_{12p2}}, \tag{12}$$

$$\beta = a\cos\left(\frac{\Delta X'_{12p1}\,(D + d_1)}{2l_1 X_0 \cos\left(a\tan\left(\frac{\Delta Y'_{12p1}}{\Delta X'_{12p1}}\right)\right)}\right). \tag{13}$$

Additionally, by (8-1), (8-2), (11), (12), and (13), the displacements Δx and Δy can be expressed, respectively, as follows:

$$\Delta x = X'_{1p1}\frac{D + d_1}{l_1} - X_0 \cos\gamma \cos\beta \tag{14}$$

$$\Delta y = Y'_{1p1}\frac{D + d_1}{l_1} - Y_0 \cos\gamma \cos\beta \tag{15}$$

Applying Eq. (5) to the projected point P'_{3p1} (generated by lens 1), the following equations hold:

$$X'_{3p1} = \frac{l_1 Y_0}{D + d_1}\left(\sin\vartheta \sin\beta \cos\gamma - \sin\gamma \cos\vartheta + \frac{\Delta x}{Y_0}\right), \tag{16-1}$$

$$Y'_{3p1} = \frac{l_1 Y_0}{D + d_1}\left(\sin\vartheta \sin\beta \sin\gamma + \cos\gamma \cos\vartheta + \frac{\Delta y}{Y_0}\right). \tag{16-2}$$

Finally, ϑ can be derived by (16-1) and (16-2), giving rise to the following expressions:

$$\vartheta = a\sin\left(\frac{B}{\sin\beta}\right), \tag{17}$$

$$B = \frac{\left(X'_{3p1} Y_0 - \Delta x Q\right)\cos\gamma + \left(Y'_{3p1} Y_0 - \Delta y Q\right)\sin\gamma}{Q Y_0},$$

$$Q = \frac{l_1 Y_0}{D + d_1}.$$

To summarize the above discussion, the solutions obtained in this section for the inverted system introduced in Sect. 3.2 are represented by relations (11), (12), (13), (14), (15), and (17). The following obvious conditions are postulated:

$$\gamma \in \left]-\frac{\pi}{2}, \frac{\pi}{2}\right[\qquad \Delta X_{12p1} \neq 0, \tag{18}$$

$$l_1 \Delta X'_{12P1} - l_2 \Delta X'_{12p2} \neq 0 \quad \left(\frac{X'_{1p1}}{l_2} \neq \frac{X'_{1p2}}{l_1}\right), \tag{19}$$

$$\beta \in]0, \pi[\,, \tag{20}$$

$$\vartheta \in \left[-\frac{\pi}{2}, \frac{\pi}{2}\right]. \tag{21}$$

It is understood that $X_0 > 0$, $Y_0 > 0$, $l_2 > l_1 \neq 0$, $d_2 > d_2 \neq 0$. It should be also noted that, due to the construction of the bifocal system, the following relations hold:

$$\Delta X'_{12p1} \neq 0, \frac{l_1 d_2 \Delta X'_{12p2} - l_2 d_1 \Delta X'_{12p1}}{l_1 \Delta X'_{12P1} - l_2 \Delta X'_{12p2}} > 0, \text{ and } l_1 \Delta X'_{12P1} - l_2 \Delta X'_{12p2} \neq 0.$$

During the algebraic manipulation carried out to obtain expression (13), it has been implicitly assumed that $-1 \leq \frac{\Delta X'_{12p1}(D+d_1)}{2l_1 X_0 \cos\gamma} \leq 1$. Therefore, expression (13) is well defined for all given values of $\Delta X'_{12p1}$ and $\Delta Y'_{12p1}$ (recall also that, by (18), $\gamma \neq \pm\frac{\pi}{2}$). Analogous considerations hold for (17) by (20). Note additionally that the existence conditions for γ can be extended considering the whole angle $[0, 2\pi\ ]$ provided that it is possible to identify, each time, the specific sub-intervals involved (e.g., $\gamma \in \left]-\frac{\pi}{2}, \frac{\pi}{2}\right[$ or $\gamma \in \left]\frac{\pi}{2}, \frac{3\pi}{2}\right[$). In any case, the conditions $\gamma \neq \pm\frac{\pi}{2}$ and $\gamma \neq \frac{3\pi}{2}$ must be satisfied. Analogous considerations hold for β, while no extension for ϑ would be of use.

3.4 Error Analysis

This section studies the impact of measurement errors, relative to the image-points, on the computation of the position and attitude of the target (by the inverse equation system corresponding to (11), (12), (13), (14), (15), and (17)). More precisely, taking a worst-case perspective, the maximum error for the terms ϑ, β, γ, D, Δx, and Δy is estimated, assuming that the absolute value of the measurement error associated with the variables X'_{1p1}, Y'_{1p1}, X'_{2p1}, Y'_{2p1}, Y'_{3p1}, X'_{1p2}, and X'_{2p2} is less than a given E. The distance D is deemed to represent the most critical aspect, especially when large distances are involved. The maximum error $|\varepsilon_D|_{max}$ with respect to the distance D is briefly discussed next.

Considering Eq. (12), the error $|\varepsilon_D|$ with respect to the actual distance D is expressed as follows:

$$|\ \varepsilon_D\ | = \left| \frac{l_1 d_2 \Delta X'_{12p2} - l_2 d_1 \Delta X'_{12p1} + l_1 d_2 \varepsilon'_{12p2} - l_2 d_1 \varepsilon'_{12p1}}{l_1 \Delta X'_{12p1} - l_2 \Delta X'_{12p2} + l_1 \varepsilon'_{12p1} - l_2 \varepsilon'_{12p2}} - D \right|, \tag{22}$$

where ε'_{12p1} and ε'_{12p2} represent the measurement errors corresponding to $\Delta X'_{12p1}$ and $\Delta X'_{12p2}$, respectively. Depending on the specific technology adopted, with the estimated maximum error E, the following bounds are considered:

$$\left|\varepsilon'_{12p1}\right| \leq E, \tag{23-1}$$

$$\left|\varepsilon'_{12p2}\right| \leq E. \tag{23-2}$$

Since $\frac{l_1 d_2 \Delta X'_{12p2} - l_2 d_1 \Delta X'_{12p1}}{l_1 \Delta X'_{12p1} - l_2 \Delta X'_{12p2}} = D$ ($D \geq 0$), and $l_1 \Delta X'_{12p1} - l_2 \Delta X'_{12p2} < 0$ ($l_2 > l_1$ and $\Delta X'_{12p2} > \Delta X'_{12p1}$ due to the way the optical system is constructed), the following relation holds:

$$|\varepsilon_D|_{max} = \max_{\vartheta,\beta,\gamma,\Delta x,\Delta y,\ \varepsilon'_{12p1},\varepsilon'_{12p2}} \left| \frac{l_1 d_2 \Delta X'_{12p2} - l_2 d_1 \Delta X'_{12p1} + l_1 d_2 \varepsilon'_{12p2} - l_2 d_1 \varepsilon'_{12p1}}{l_1 \Delta X'_{12p1} - l_2 \Delta X'_{12p2} + l_1 \varepsilon'_{12p1} - l_2 \varepsilon'_{12p2}} - D \right|, \tag{24}$$

where ϑ, β, γ, Δx, Δy vary within given intervals (delimiting the roto-translations to consider). To find a first approximation $\left|\widetilde{\varepsilon_D}\right|_{max}$ for (24) (by involving a reduced number of variables), the following terms are introduced:

$$\eta_D^- = \max_{\vartheta,\beta,\gamma,\Delta x,\Delta y,\Delta z} \left\{ D - \frac{l_1 d_2 \Delta X'_{12p2} - l_2 d_1 \Delta X'_{12p1} + l_1 d_2 E + l_2 d_1 E}{l_1 \Delta X'_{12p1} - l_2 \Delta X'_{12p2} - l_1 E - l_2 E} \right\}, \tag{25-1}$$

$$\eta_D^+ = \max_{\vartheta,\beta,\gamma,\Delta x,\Delta y,\Delta z} \left\{ \frac{l_1 d_2 \Delta X'_{12p2} - l_2 d_1 \Delta X'_{12p1} - l_1 d_2 E - l_2 d_1 E}{l_1 \Delta X'_{12p1} - l_2 \Delta X'_{12p2} + l_1 E + l_2 E} - D \right\}. \tag{25-2}$$

Here we assume $\frac{l_1 d_2 \Delta X'_{12p2} - l_2 d_1 \Delta X'_{12p1} + l_1 d_2 E + l_2 d_1 E}{l_1 \Delta X'_{12p1} - l_2 \Delta X'_{12p2} - l_1 E - l_2 E} > 0$, and $\frac{l_1 d_2 \Delta X'_{12p2} - l_2 d_1 \Delta X'_{12p1} - l_1 d_2 E - l_2 d_1 E}{l_1 \Delta X'_{12p1} - l_2 \Delta X'_{12p2} + l_1 E + l_2 E} > 0$. The approximate term $\left|\widetilde{\varepsilon_D}\right|_{max}$ ($\left|\widetilde{\varepsilon_D}\right|_{max} > |\varepsilon_D|_{max}$) is thus expressed as

$$\left|\widetilde{\varepsilon_D}\right|_{max} = \max\left\{\eta_D^-, \eta_D^+\right\}. \tag{26}$$

Let us remark that more than one single critical roto-translation in (24) or (26) could occur that gives rise to the maximum error: for example, due to symmetrical conditions. The issue of identifying the whole set of critical roto-translations is not trivial, and it is not considered in this chapter: it could be the subject of further research.

4 Optimization Aspects

Mathematical optimization models have been introduced in Sect. 3.4 concerning the error analysis of the studied optical system. There, a worst-case approach is adopted to estimate the maximum possible error with respect to the distance D (due to measurement errors relative to the projection differences $\Delta X'_{12p1}$ and $\Delta X'_{12p1}$

associated with lenses 1 and 2, respectively). In this section, two optimization problems are discussed with the scope of maximizing the overall performances of the bifocal system illustrated in this chapter. The first optimization problem, discussed in Sect. 4.1, is aimed at finding the size of the optical head so that the error with respect to distance D becomes as small as possible.

The second optimization problem concerns the specific features of the light spots utilized as the target image for the bifocal system. In fact, the light spots are not idealized geometrical points (as assumed in the mathematical formulation of Sect. 3), but they have an actual size. Therefore, each light spot is identified as a surface by the image sensor (CCD). In general, the light energy intensity on this surface does not have a uniform distribution. The concept of light spot centroid is introduced to represent the distribution of the light energy intensity on the light spot surface. This concept is the equivalent to the center of mass for a mass distribution in a geometric domain. Each light spot centroid is identified with one of the three single light points utilized by the bifocal system, to determine the roto-translation of the whole target as discussed in Sect. 3. In general, a roto-translation of the target yields a variation in the light energy intensity distribution on the surface of each light spot. The position of each light spot centroid typically varies as well with respect to the CCD. This centroid displacement is thus due to not only the actual roto-translation of the whole target, but also to the change in the light energy intensity distribution on the light spot surface. Therefore, the centroid displacement on each light spot surface, obtained after a roto-translation of the target, also depends on the light energy intensity distribution of the spot before the roto-translation. If the roto-translations of the target are limited with respect to the initial (nominal) condition, then the light energy intensity distribution of each light spot in the nominal condition can be properly shaped a priori, to minimize the centroid displacement. Consequently, under these proximity conditions, the precision of the bifocal metrological approach is maximized. This optimization aspect is discussed in Sect. 4.2.

4.1 System Sizing Optimization

The maximum error $|\varepsilon_D|_{max}$ related to the distance D, as expressed by (24) depends implicitly also on the following parameters that characterize the bifocal system: d_1, d_2 (corresponding to $D + d_1$, $D + d_2$ working distances of lenses 1 and 2, respectively), l_1, l_2 (internal optical lengths of lenses 1 and 2, respectively), and f_1, f_2 (focal distances of lens 1 and 2, respectively). These parameters can vary within their ranges: $d_1 \in \left[\underline{D_1}, \overline{D_1}\right]$, $d_2 \in \left[\underline{D_2}, \overline{D_2}\right]$, $l_1 \in \left[\underline{L_1}, \overline{L_1}\right]$, $l_2 \in \left[\underline{L_2}, \overline{L_2}\right]$, $f_1 \in \left[\underline{F_1}, \overline{F_1}\right]$, $f_2 \in \left[\underline{F_2}, \overline{F_2}\right]$, where $\underline{D_1}$, $\underline{D_2}$, $\underline{L_1}$, $\underline{L_2}$, $\underline{F_1}$, $\underline{F_2}$ and $\overline{D_1}$, $\overline{D_2}$, $\overline{L_1}$, $\overline{L_2}$, $\overline{F_1}$, $\overline{F_2}$ are the lower and upper technological bounds. Next, the following *minimax* optimization problem is considered:

$$|\overline{\varepsilon_D}|_{\min} = \min_{d_1,d_2,l_1,l_2,f_1,f_1}\left\{\max_{\vartheta,\beta,\gamma,\Delta x,\Delta y,\varepsilon'_{12p1},\varepsilon'_{12p2}}\left|\frac{l_1d_2\Delta X'_{12p2}-l_2d_1\Delta X'_{12p1}+l_1d_2\varepsilon'_{12p2}-l_2d_1\varepsilon'_{12p1}}{l_1\Delta X'_{12p1}-l_2\Delta X'_{12p2}+l_1\varepsilon'_{12p1}-l_2\varepsilon'_{12p2}}-D\right|\right\}. \tag{27}$$

Here, $|\overline{\varepsilon_D}|_{\min}$ is the minimum error related to the distance D, with respect to the parameters d_1, d_2, l_1, l_2, f_1, and f_2, in the worst case as expressed by (24). Considering the difficulty of this optimization problem, especially if a global optimization point of view is adopted (see, e.g., [5, 8, 11]), the variables ϑ, β, γ, Δx, Δy, ε'_{12p1}, ε'_{12p2}, and ε'_{12p2} can be fixed in (27) at the values obtained by solving optimization problem (24). This implies that problem (27) can be simplified as follows:

$$|\overline{\varepsilon_D}|_{\min} = \min_{d_1,d_2,l_1,l_2,f_1,f_1}\left\{\left|\frac{l_1d_2\Delta X'_{12p2}-l_2d_1\Delta X'_{12p1}+l_1d_2\varepsilon'_{12p2}-l_2d_1\varepsilon'_{12p1}}{l_1\Delta X'_{12p1}-l_2\Delta X'_{12p2}+l_1\varepsilon'_{12p1}-l_2\varepsilon'_{12p2}}-D\right|\right\}, \tag{28}$$

where only d_1, d_2, l_1, l_2, f_1, f_1 are considered as variables, while $\Delta X'_{12p2}$, $\Delta X'_{12p1}$, ε'_{12p2}, $\varepsilon\prime_{12p1}$ take instead the values corresponding to the worst-case solution provided by (24). In this framework it is implicitly assumed that exclusively the critical roto-translation corresponding to the solution obtained for (24) is considered. If the number of critical roto-translations providing the same error $|\varepsilon_D|_{\max}$ as the solution of (24) is available, then it is possible to properly extend optimization problem (28) in order to consider all of these. For this purpose, the error

$$(|\overline{\varepsilon_D}|)_\alpha = \left|\frac{l_1d_2\Delta X'_{12p2}-l_2d_1\Delta X'_{12p1}+l_1d_2\varepsilon'_{12p2}-l_2d_1\varepsilon'_{12p1}}{l_1\Delta X'_{12p1}-l_2\Delta X'_{12p2}+l_1\varepsilon'_{12p1}-l_2\varepsilon'_{12p2}}-D\right|_\alpha$$

can be associated with each critical roto-translation solution α (fixing the corresponding values ϑ, β, γ, Δx, Δy, ε'_{12p1}, ε'_{12p2} obtained from (24)). The extended optimization problem can be then expressed as $\min_{d_1,d_2,l_1,l_2,f_1,f_1}\sum_\alpha(|\overline{\varepsilon_D}|)_\alpha$.

4.2 Light Spot Optimization

In this section, first we recall the concept of light spot centroid: then the spot optimization model is formulated. As we pointed out, the concept of centroid in optical metrology is analogous to that of the center of mass relative to a continuous mass distribution within a given domain. As is known, this is formulated as follows:

$$u_c = \frac{\int_S u_\beta\rho(u)du}{\int_S\rho(u)du}. \tag{29}$$

Here, u_c is the center of mass, in the three-dimensional case u_β with $\beta = 1$, 2, 3 are the coordinates in the given reference frame, S is the continuous domain,

and $\rho(u)$ is the associated density function. In the optical context, an analogous expression holds, when the mass density is replaced by the light energy intensity $I(u)$. Regarding the discretized image created on the CCD, the following two-dimensional light intensity centroid is introduced:

$$X_{\mathrm{c}} = \frac{\sum_{i,j} X_{ij} I\left(X_{ij}, Y_{ij}\right)}{I_{\mathrm{T}}}, \qquad Y_{\mathrm{c}} = \frac{\sum_{i,j} Y_{ij} I\left(X_{ij}, Y_{ij}\right)}{I_{\mathrm{T}}}. \tag{30}$$

Here, $(X_{ij}, Y_{ij}) \in \mathbb{N}_0 \times \mathbb{N}_0$ (denoting non-negative integer coordinates) are the points (pixels) representing the CCD (discretized) domain with respect to a given orthogonal reference frame (O, X, Y) associated with the CCD. The integer-valued function $I(X_{ij}, Y_{ij}) \in \mathbb{N}$ is the light energy intensity. Without loss of generality, it is assumed that $(X_{00}, Y_{00}) = (0, 0)$, and that $X_{ij}, Y_{ij} \geq 0$ holds for all pairs i, j. Any roto-translation of a target (consisting of light spots) generates, in general, a displacement in the corresponding light spot centroids. Therefore, considering a general light spot, the relative centroid displacement with respect to the CCD reference frame coordinates is expressed as follows:

$$\Delta X_{\mathrm{c}} = \left| \frac{\sum_{ij} X_{ij} I_{ij} - \sum_{ij} X_{ij} I'_{ij}}{I_{\mathrm{T}}} \right|, \qquad \Delta Y_{\mathrm{c}} = \left| \frac{\sum_{ij} Y_{ij} I_{ij} - \sum_{ij} Y_{ij} I'_{ij}}{I_{\mathrm{T}}} \right|. \tag{31}$$

Here, I_{ij} and I'_{ij} represent (with a simplified notation) the intensities $I(X_{ij}, Y_{ij})$ and $I'(X_{ij}, Y_{ij})$ before and after the centroid displacement, respectively. Moreover, $I_T \equiv \sum I_{ij}$ with the intensity conservation condition shown below:

$$\sum_{ij} I_{ij} = \sum_{ij} I'_{ij}. \tag{32}$$

Therefore, the overall Euclidean centroid displacement is

$$\Delta_{\mathrm{c}} = \frac{1}{I_{\mathrm{T}}} \sqrt{\Delta X_{\mathrm{c}}{}^2 + \Delta Y_{\mathrm{c}}{}^2}. \tag{33}$$

In the following, it is assumed that the light spots corresponding to the initial target position and attitude with respect to the bifocal system can be generated so that their intensity distributions are identical to each other. Therefore, the optimization problem discussed here focuses on a single light spot. Its initial intensity distribution $w(X_{ij}, Y_{ij}) \in \mathbb{N}$, expressed in bit units and referred to in the following as the nominal state, is considered together with a changed state $w'(X_{ij}, Y_{ij}) \in \mathbb{N}$ (also expressed in bit units). In the following, these notations are simplified as w_{ij} and w'_{ij}. The changed state w'_{ij} corresponds to an overall intensity distribution variation, considered as representative of the perturbations of the nominal light spot in a limited neighborhood of the initial conditions.

The objective of the optimization approach proposed is to determine an intensity distribution w_{ij} for the nominal light spot to minimize the overall centroid displacement, as expressed by (33) corresponding to the perturbed intensity state w'_{ij}. Moreover, we want to determine the intensity distribution w_{ij} so that it is highly "regular," symmetrical with respect to the centroid and strongly concentrated around it (while vanishing as more external areas are reached). The function $w'_{ij} = f_{ij}\left(w_{ij}, \vartheta, \beta, \gamma, \Delta x, \Delta y, \Delta z\right)$ that, for each (X_{ij}, Y_{ij}), associates the perturbed intensity w'_{ij} with the nominal intensity w_{ij} and the general roto-translation ϑ, β, γ, Δx, Δy, Δz (recall Sect. 3) is very difficult to express mathematically.

Observe that considering all possible perturbations (ϑ, β, γ, Δx, Δy, Δz) in a limited neighborhood of the nominal condition (corresponding to $\vartheta = 0$, $\beta = 0$, $\gamma = 0$, $\Delta x = 0$, $\Delta y = 0$, $\Delta z = 0$) would lead to a challenging *minimax* problem. These aspects are therefore omitted in the model discussed here, providing instead a simplified approximate formulation of the problem. This model is expressed in terms of mixed integer linear programming (MILP), consult, e.g., Hillier [7], Minoux [9], and Nemhauser [10]. The convention of using capital letters for constants and lower-case letters for variables is adopted henceforth.

A discretized domain (sub-domain of the CCD containing the light spot) is described by the integer coordinates (X_{ij}, Y_{ij}) assuming that $i \in [0, N]$, $j \in [0, N]$, and N is an even integer. The perturbed intensity distribution w'_{ij} is supposed to be determined by imposing that $\forall i, j \quad \left|w_{ij} - w'_{ij}\right| \leq \overline{\Delta W}$ and $\sum_{ij} \left|w_{ij} - w'_{ij}\right| = P_{\mathrm{T}}$, with $\overline{\Delta W}$ and P_{T} as appropriately chosen positive constants, in addition to the total intensity conservation Eq. (32) applied to w_{ij} and $w'_{ij,}$, i.e., $\sum_{ij} w = \sum_{ij} w\prime_{ij}$. All this is, as a matter of fact, just a simplifying trick to avoid the non-trivial challenge of expressing the actual function $w'_{ij} = f_{ij}\left(w_{ij}, \vartheta, \beta, \gamma, \Delta x, \Delta y, \Delta z\right)$ explicitly, as well as of dealing with a far more challenging *minimax* problem. The resulting formulation is therefore a surrogate model, defined in order to provide approximate practical solutions, while removing excessive complexity.

Following this approach, in addition to the intensity conservation condition (32), we assume that it is possible to choose $\overline{\Delta W}$and P_{T} so that the conditions listed above can realistically condition the intensity distributions w'_{ij} as approximately representative of all considered perturbations. In this perspective, these conditions, acting on the intensity variations both at a pixel and at an overall level, can be interpreted as a relaxation of the constraint $w'_{ij} = f_{ij}\left(w_{ij}, \vartheta, \beta, \gamma, \Delta x, \Delta y, \Delta z\right)$ and a significant simplification of the original *minimax* problem. The values for $\overline{\Delta W}$and P_{T} have to be estimated a priori, and this necessarily entails some arbitrariness. For instance, these parameters could be chosen bearing in mind the most critical or the most frequent cases. In general, different estimations lead to diverse solutions for the intensity distribution w_{ij} of the nominal light spot. The alternative solutions obtained can be compared to each other, to select (by means of dedicated numerical simulations) the most suitable scenario from a practical point of view.

Considering all aspects stated above, the simplified model is formulated next, explaining step by step the meaning of the expressions involved. First, the binary variables $\sigma_{ij} \in \{0, 1\}$, $\delta_{ij}^{-} \in \{0, 1\}$, and $\delta_{ij}^{+} \in \{0, 1\}$ are defined as follows:

$$\begin{aligned} &\sigma_{ij} = 1 \text{ if pixel } (i, j) \text{ is active } \left(\text{i.e., } w_{ij} > 0\right) \\ &\sigma_{ij} = 0 \text{ otherwise,} \end{aligned}$$

$$\begin{aligned} &\delta_{ij}^{-} = 1 \text{ if } w_{ij} > w'_{ij}, \\ &\delta_{ij}^{-} = 0 \text{ otherwise,} \end{aligned}$$

$$\begin{aligned} &\delta_{ij}^{+} = 1 \text{ if } w_{ij} < w'_{ij}, \\ &\delta_{ij}^{-} = 0 \text{ otherwise.} \end{aligned}$$

Here $w_{ij}, w'_{ij} \in \mathbb{N}_0$.

The variables $d_{ij}^{-} \in \mathbb{N}_0$ and $d_{ij}^{+} \in \mathbb{N}_0$are defined next as follows:

$$\begin{aligned} &d_{ij}^{-} = w_{ij} - w'_{ij} \text{ if } w_{ij} > w'_{ij}, \\ &d_{ij}^{-} = 0 \qquad\quad \text{otherwise,} \end{aligned}$$

$$\begin{aligned} &d_{ij}^{+} = w'_{ij} - w_{ij} \text{ if } w_{ij} < w'_{ij}, \\ &d_{ij}^{+} = 0 \qquad\quad \text{otherwise.} \end{aligned}$$

The variables σ_{ij}, δ_{ij}^{-}, δ_{ij}^{+}, d_{ij}^{-}, and d_{ij}^{+} are interrelated as shown below:

$$\forall i, j \quad \delta_{ij}^{-} + \delta_{ij}^{+} \leq \sigma_{ij}, \tag{34}$$

$$\forall i, j \quad d_{ij}^{-} \geq \underline{\Delta W} \delta_{ij}^{-}, \tag{35-1}$$

$$\forall i, j \quad d_{ij}^{+} \geq \underline{\Delta W} \delta_{ij}^{+}, \tag{35-2}$$

$$\forall i, j \quad d_{ij}^{-} \leq \overline{\Delta W} \delta_{ij}^{-}, \tag{36-1}$$

$$\forall i, j \quad d_{ij}^{+} \leq \overline{\Delta W} \delta_{ij}^{+}. \tag{36-2}$$

Here the positive integers $\underline{\Delta W}$and $\overline{\Delta W}$ represent the minimum and maximum admissible intensity change, expressed in bit units, for each active pixel (i,j). The lower bounds (35-1) and (35-2) are introduced to easily realize detectable changes in the intensity distribution w'_{ij}. The following lower and upper bounds hold for both the nominal and perturbed states w_{ij} and w'_{ij}, respectively, in each active pixel:

$$\forall i,\, j \qquad w_{ij} - d_{ij}^{-} \geq \underline{W}\sigma_{ij}, \tag{37-1}$$

$$\forall i,\, j \qquad w_{ij} + d_{ij}^{+} \leq \overline{W}\sigma_{ij}. \tag{37-2}$$

Here the positive integers $\underline{W}$and $\overline{W}$ represent the minimum and maximum admissible intensity associated with each pixel (i,j). From (37-1) and (37-2) it can also be observed that all active pixels in the nominal condition coincide with the active pixels of the perturbed state: this way, the overall shape of the light spot remains unaltered.

The next condition represents the overall intensity perturbation imposed, expressed again in bit units:

$$\sum_{ij} \left(d_{ij}^{-} + d_{ij}^{+} \right) = P_{\mathrm{T}} \tag{38}$$

Here P_{T} is a positive integer.

The overall intensity (W_{T}) conservation condition, involving both the nominal and the perturbed states w_{ij} and w'_{ij}, is formulated as:

$$W_{\mathrm{T}} = \sum_{ij} w_{ij} = \sum_{ij} w'_{ij}. \tag{39}$$

As a reasonable general condition, the intensity distribution w_{ij} is expected to approximate a bell-shaped continuous function with compact support. (For a similar shape, one can think of an appropriately truncated normal distribution.) The conditions introduced next pursue this overall shape by regularity and symmetry criteria. Specifically, the conditions given below determine a monotonically increasing or decreasing trend, with respect to the central pixel $\left(\hat{i},\, \hat{j}\right)$for the nominal intensity distribution w_{ij}:

$$\forall i,\, j \mid i < \hat{i} - 1 \qquad w_{ij} + \underline{DW}\sigma_{ij} \leq w_{i+1,j}, \tag{40-1}$$

$$\forall j \qquad w_{\hat{i}-1,j} \leq w_{\hat{i}j}, \tag{40-2}$$

$$\forall j \qquad w_{\hat{i}+1,j} \leq w_{\hat{i}j}, \tag{40-3}$$

$$\forall i, j \mid i > \hat{i} + 1 \qquad w_{ij} - \underline{DW}\sigma_{ij} \geq w_{i+1,j}, \tag{40-4}$$

$$\forall i, j \mid j < \hat{j} - 1 \qquad w_{ij} + \underline{DW}\sigma_{ij} \leq w_{i,j-1}, \tag{40-5}$$

$$\forall i \qquad w_{i,\hat{j}-1} \leq w_{i\hat{j}}, \tag{40-6}$$

$$\forall i \qquad w_{i,\hat{j}+1} \leq w_{i\hat{j}'} \tag{40-7}$$

$$\forall \mathrm{i}, j \mid j > \hat{j} + 1 \qquad w_{ij} - \underline{DW}\sigma_{ij} \geq w_{i,j+1}. \tag{40-8}$$

Here, $\hat{i}, \hat{j} = \frac{N}{2}$, and the positive integer $\underline{DW}$ is the minimum intensity increment/decrement (expressed in bit units) corresponding to two adjacent indices $i, i + 1$ or $j, j + 1$, except for the indices immediately adjacent to $\hat{i}$ and $\hat{j}$. The following "Lipschitzian" conditions are further imposed to the nominal intensity distribution w_{ij} to prevent sudden increments/decrements in adjacent indices:

$$\forall i, j \mid i < \hat{i} \quad w_{i+1,j} - w_{\mathrm{i}j} \leq \overline{DW}, \tag{41-1}$$

$$\forall i, j \mid i > \hat{i} \quad w_{ij} - w_{i+1,j} \leq \overline{DW}, \tag{41-2}$$

$$\forall i, j \mid j < \hat{j} \quad w_{i,j+1} - w_{ij} \leq \overline{DW}, \tag{41-3}$$

$$\forall i, j \mid j > \hat{j} \quad w_{ij} - w_{i,j+1} \leq \overline{DW}, \tag{41-4}$$

where $\overline{DW}$ is an appropriate bound, compliant with the given technological restrictions.

Several "weak" symmetry conditions are introduced additionally, to induce a desired overall trend of the nominal intensity distribution $w_{i,j}$. Their formulation is shown below:

$$\forall j \quad w_{0j} = w_{Nj}, \tag{42-1}$$

$$\forall j \quad w_{\hat{i}-1,j} = w_{\hat{i}+1,j}, \tag{42-2}$$

$$\forall j \quad \sum_{i<\hat{i}} w_{ij} = \sum_{i>\hat{i}} w_{ij}, \tag{42-3}$$

$$\forall i \quad w_{i0} = w_{iN}, \tag{42-4}$$

$$\forall i \quad w_{i,\hat{j}-1} = w_{i,j+1}, \tag{42-5}$$

$$\forall i \quad \sum_{j<\hat{j}} w_{ij} = \sum_{j>\hat{j}} w_{ij}. \tag{42-6}$$

To consider realistic scenarios, it can be further imposed that all the pixels corresponding to non-decreasing intensity with respect to the nominal distribution (i.e., $w'_{ij} \geq w_{ij}$) delimit convex areas of the domain (X_{ij},Y_{ij}). For example, additional conditions such as $\forall i, j \ \sum_{\bar{i}>i,j} d_{ij}^{-} \leq N^2 \left(1 - \delta_{ij}^{+}\right)$ can be introduced. These conditions express the property that from a certain index i (not determined a priori) all subsequent pixels with index $\bar{i} > i$ have a non-decreasing intensity and vice versa. (However, these aspects are not discussed in this chapter.)

Since in any real context the intensity is expected to be maximal in a central area of the spot, this criterion is selected as the optimization objective. The overall centroid displacement is instead bounded by the following inequalities:

$$\frac{\sum_{ij} X_{ij} w_{ij} - \sum_{ij} X_{ij} w'_{ij}}{W_{\mathrm{T}}} \leq \overline{\Delta}_{\mathrm{C}}, \tag{43-1}$$

$$\frac{\sum_{ij} Y_{ij} w_{ij} - \sum_{ij} Y_{ij} w'_{ij}}{W_{\mathrm{T}}} \leq \overline{\Delta}_{\mathrm{C}}, \tag{43-2}$$

Here $\overline{\Delta}_{\mathrm{C}}$ is an appropriate estimation of the maximum acceptable displacement for the centroid. Finally, the following optimization criterion is introduced:

$$\max \sum_{(i,j)\in A_{\mathrm{C}}} w_{ij}. \tag{44}$$

where A_{C} represents a proper central area.

It can be observed that the model solutions are necessarily related to the choice of the parameters $\overline{\Delta W}$ and P_{T}, assumed to represent the specific case under study. As anticipated, a number of different choices can be compared to select the most suitable option from a practical point of view. This approach could however be significantly improved by adopting a multi-scenario optimization point of view. In this perspective, instead of $\overline{\Delta W}$ and P_{T} a set of parameters $\overline{\Delta W}_{\alpha}$ and $P_{\mathrm{T}\alpha}$ ($\alpha = 1, \ldots, N_{\mathrm{S}}$) are considered. A perturbed intensity $w'_{ij\alpha}$ is associated with the corresponding parameters $\overline{\Delta W}_{\alpha}$ and $P_{\mathrm{T}\alpha}$, and the whole model is extended by properly replicating and readjusting the conditions and the objective function involved. However, this aspect – as a possible topic of future research – is not investigated here.

5 An Illustrative Case Study

As mentioned in Sect. 1, the bifocal system has recently been considered for possible utilization for the Athena satellite. The case study is only briefly outlined here, omitting (for confidentiality reasons) most of the technical details.

The two instruments, high-resolution X-ray Integral Field Unit (X-IFU) and Wide Field Imager (WFI) mentioned in Sect. 1, are accommodated within the Focal Plane Module (FPM). The Mirror Assembly Module (MAM) is placed at an assigned distance (12 m) from the FPM. Since the telescope line of sight is determined by the telescope mirror position and attitude, the on-board metrology is aimed at supporting the active control of the MAM focal point position with respect to the FPM instruments. The proposed design for the bifocal metrology on board Athena considers:

- The bifocal optical head mounted on the MAM and aligned with it
- One light target on each instrument

The overall light target is essentially composed by three LEDs defining an isosceles triangle. With reference to this specific case study, three main aspects have been investigated in depth (by applying the concepts discussed in Sects. 3.4, 4.1 and 4.2):

- Error analysis for the measured distance between the MAM focal point position and the FPM instruments
- Optimal system sizing
- Light spot optimization

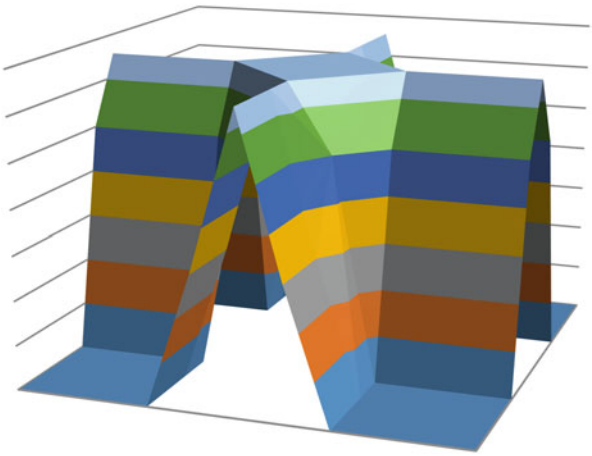

Fig. 11 Case study: nominal intensity distribution example 1

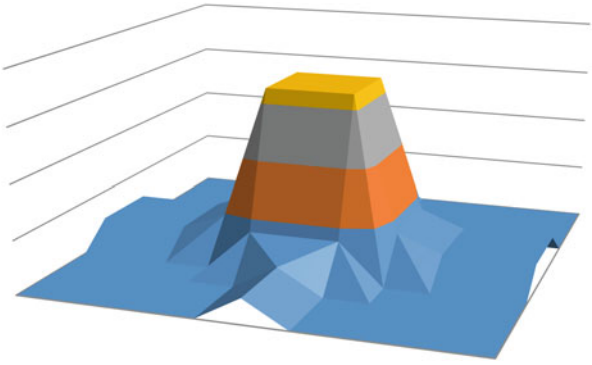

Fig. 12 Case study: nominal intensity distribution example 2

The optimization models considered for both error analysis and system sizing have been solved by the global-local nonlinear optimization software package LGO [12]. Again, technical details are not reported here for confidentiality reasons. As a main result, a trade-off concerning the optimal focal distances f_1 and f_2 has been made. On the one hand, these terms should be close to each other ($f_1 \sim f_2$) and as large as possible, compatibly with the maximum admissible dimension of the optical head. On the other hand, a small difference between f_1 and f_2 can give rise to possible partial overlapping between the light spot projections on the CCD.

The MILP model adopted for the light spot optimization has been solved by the IBM ILOG CPLEX solver (version 12.3). Several possible solutions have been considered. Figures 11 and 12 illustrate two examples of optimal nominal light spots obtained for the case study (the physical units have been omitted for confidentiality reasons).

6 Concluding Remarks

The work presented here discusses an innovative metrological approach, based on a recently patented bifocal optical system [2–4]. This system is aimed at measuring the position and attitude of a target item, identified by means of three light spots, almost instantaneously and with high precision. The approach proposed is simple and efficient: here it is discussed in relation to advanced space engineering applications, but not limited to these.

In this chapter, the concept of the bifocal optical system is discussed in depth, investigating some mathematical aspects relevant the overall methodology adopted, including error analysis, system sizing optimization, and light spot optimization. Finally, a real-word case study is highlighted.

Future research can be aimed at advancements in relation to both the error analysis and system sizing optimization problems discussed here. In this perspective, enhancements of the global optimization approach followed aimed at improving the global search can be expected. Concerning the light spot optimization problem, to extend solution adaptability and reliability, the corresponding MILP model could be considered in a multi-scenario optimization approach.

References

1. Bresciani, F. (2016) An innovative bifocal metrology system for aerospace applications. Journal of Instrumentation, Vol. 11, 4th International Conference Frontiers in Diagnostics Fix Technologies (ICFDT4).
2. Bresciani F., Musso, F. (2015) Projective optical metrology system for determining attitude and position. IT007-BIS EP2508427 (Patent granted in EP and USA).
3. Bresciani, F., Musso, F. (2016) Coarse and fine projective optical metrology system IT007 EP2508428 (Patent granted in EP and USA).
4. Bresciani, F., Musso, F. (2017) Projective optical metrology system. IT008 EP2677338 (Patent granted in EP and USA).
5. Floudas, C.A. and Pardalos P.M., Eds. (2001) *Encyclopedia of Optimization*. Kluwer Academic Publishers, Dordrecht, The Netherlands.
6. Ghali, S. (2008) *Introduction to Geometric Computing.* Springer Science + Business Media, New York.
7. Hillier, F.S. and Lieberman, G.J. (2001) *Introduction to Operations Research.* McGraw-Hill, New York.
8. Liberti, L., Maculan, N., (Eds.) (2005) *Global Optimization: From Theory to Implementation.* Springer Science + Business Media, New York.
9. Minoux, M. (1986) *Mathematical Programming: Theory and Algorithms.* John Wiley & Sons, Paris.
10. Nemhauser, G.L., Wolsey, L.A. (1988) *Integer and Combinatorial Optimization.* Wiley, New York.
11. Pintér, J.D. (1996) *Global Optimization in Action.* Kluwer Academic Publishers, Dordrecht, The Netherlands. Available from Springer Science + Business Media, New York.
12. Pintér, J.D. (2015) *LGO – A Model Development and Solver System for Global-Local Nonlinear Optimization. User's Guide.* PCS Inc., Canada.

13. Tyson, R.K. (2010) *Principles of Adaptive Optics*. Taylor & Francis Group (3rd ed.). CRC Press, Boca Raton, FL.
14. Yoshizawa, T. (Ed.). (2015) *Handbook of Optical Metrology*. *Principles and Applications*. Taylor & Francis Group (2nd ed.). CRC Press, Boca Raton, FL.